Top Catal (2012) 55:322–335
DOI 10.1007/s11244-012-9800-8

ORIGINAL PAPER

Evolution of Pt and Pt-Alloy Catalytic Surfaces Under Oxygen Reduction Reaction in Acid Medium

P. B. Balbuena · R. Callejas-Tovar · P. Hirunsit · J. M. Martínez de la Hoz · Y. Ma · G. E. Ramírez-Caballero

Published online: 20 April 2012

Abstract We review our recent work that employs a series of computational techniques including density functional theory, ab initio molecular dynamics, and classical molecular dynamics to investigate changes in the structure and electronic properties of Pt-based alloy catalysts under oxygen reduction reaction conditions in acid medium. We show density-functional theory-based correlations between surface segregation and the oxidation state of the subsurface atoms, and their effects on metal dissolution. Since the onset of Pt dissolution coincides with that of surface oxidation, surface reconstruction phenomena is evaluated using ab initio and classical molecular dynamics at increasing degrees of oxidation on extended surfaces and nanoparticles, including the effects of water and an acidic solution. Significant reconstruction and compositional changes are observed as the surface is modified by the presence of adsorbates and electrolyte components. Finally we discuss the consequences of dealloying and suggest an explanation for the enhanced activity observed experimentally in the resultant nanoporous structures.

Keywords Density functional theory · Surface oxidation · Buckling of surface atoms · Metal dissolution · Catalyst evolution · Molecular dynamics

P. B. Balbuena (✉) · R. Callejas-Tovar · P. Hirunsit · J. M. Martínez de la Hoz · Y. Ma · G. E. Ramírez-Caballero
Department of Chemical Engineering, and Materials Science and Engineering Program, Texas A&M University, College Station, TX 77843, USA
e-mail: balbuena@tamu.edu

Present Address:
G. E. Ramírez-Caballero
Departamento de Ingeniería Química, Universidad Industrial de Santander, Bucaramanga, Colombia

1 Introduction

Due to its role in electrochemical energy conversion devices, especially for transportation applications, the electrocatalytic reduction of oxygen remains one of the most outstanding challenges in electrochemical science and technology. Despite many efforts, clear understanding of the complex reaction mechanisms and achieving the goal of a highly active and stable catalyst material for the oxygen reduction reaction (ORR) at the acid conditions of low temperature proton exchange membrane fuel cells (PEMFCs) have not been fully achieved [1, 2]. In order to meet the targets for automotive use, further developments are required to improve the efficiency of the fuel cell materials, including the durability and activity of the electrocatalyst which facilitates the ORR in the cell cathode [3, 4]. Pure platinum has repeatedly been found the best catalyst for the ORR in acid medium; however, it is expensive and scarce, hindering the commercial implementation of fuel cells in automobiles. Therefore, many scientific efforts are focused in designing cheaper, more active and durable electrocatalysts than pure Pt [5].

Density functional theory (DFT) is nowadays widely used as a tool to predict the trends of catalytic activity, stability and design of catalytic and electrocatalytic materials [6–11]. DFT calculations have been found extremely useful for determination of suitable indicators of ORR electrocatalyst activity [6]. Such indicators include binding energies of the main reaction intermediates: O, OH, and OOH based on the correlation found between the oxygen reduction currents and the oxygen adsorption strengths, and due to the role of OH as a blocking species for the ORR [12–15]. Other studies have focused on elucidating reaction mechanisms using a variety of approaches from cluster models [16–21] to slab surfaces [15, 22–30]. Under the

electrochemical environment, the main changes induced by the electrode potential are manifested as surface and adsorbates polarization, and due to the presence of the solvent, the so-called electrochemical double layer which modifies the reaction conditions [31]. Several years ago, we introduced one of the first attempts to characterize such electrochemical environment [22, 23]. Our approach was very simple: surface polarization is induced by adding an excess electron to the surface and observing the evolution of the sequence of elementary ORR reactions under these conditions using ab initio Car-Parrinello molecular dynamics simulations, with the simulation cell remaining neutral by the introduction of a background charge [22]. We then repeated such simulations introducing a hydrated proton and an excess electron on the surface and again following the sequence of events with the polarized surface [23]. A more effective and less-expensive approach for introducing the effect of the electrode potential was presented by Norskov et al. [15]. In their methodology the reaction free energies are evaluated on the basis of adsorption energies of reactants and products, and then corrected by a term which represents the electrode energy at a given electrochemical potential. Such term modifies the potential energy surface for the electron transfer reactions. The results were very useful to explain trends of different ORR catalytic surfaces. In other approaches the variation of the electrode potential is represented by a variable number of electrons [32] adding complexity to the numerical calculations. However, comparison with the simpler method of Norskov and coworkers [33] shows negligible differences for the reactions tested.

Typical ORR catalysts are nanoparticles supported on a conductive medium (generally carbon). Therefore other questions arise such as what is the role of particle size and shape on the catalytic activity [34, 35], and for the DFT modelers what is the best approach to modeling the surface [36]. Modeling nanoparticles as those typically used as ORR electrocatalysts could be done representing the surface with a cluster or a slab. The question of the transition from molecular to bulk behavior has been recently addressed [37, 38]. It was concluded that the typical extended surface representation should work well for particle sizes of about 2.5 nm or larger, provided the effects of temperature and pressure are taking into account in the modeling [37]. Another factor is surface composition: Pt-based alloys have been studied for a long time aiming to substitute the platinum surface with a cheaper composite material with similar activity [4]. The main problems associated with this approach are based on the constant evolution of the surface due to surface segregation effects on alloys [39–45] which result in different surface compositions and metal dissolution reactions taking place in acid medium. For the prediction of stability of the surface electrocatalytic material, DFT calculations may be used to calculate the electrochemical potential shift (ΔU, in V) corresponding to the onset of Pt dissolution relative to that on Pt (111) surface which is used to predict the relative stability of the Pt surface atoms, in vacuum and under oxygen, for the reaction $Pt \rightarrow Pt^{+2} + 2e^{-}$ in acid medium [46–48].

Pt-skin surfaces consisting of a monolayer deposited over a substrate (single or mixed metal) are a popular electrocatalyst concept that is having a considerable impact on PEMFC catalysis due to the activity improvement observed in these materials in comparison with pure Pt [12, 49–54]. The reason of the activity improvement of Pt skin systems is related to the substantial geometric and electronic modification induced by the substrate on the physical properties of the monolayer [26, 55]. These effects include the chemical interaction between substrate and surface elements and the stress induced by the lattice constant mismatch between both regions. The topic has been the subject of numerous experimental and theoretical studies [11, 26, 43, 53–55]. However, the catalytic activity is not useful if the lifetime of the catalyst is very short. Therefore the stability of the ORR electrocatalytic material during its performance is of fundamental importance since the feasibility of a catalyst would only be firmly assessed by the combination of activity and durability properties. In this paper, we review our work related to the evolution of core–shell electrocatalysts under reaction conditions using a multiscale modeling approach involving DFT calculations as well as ab initio and classical molecular dynamics simulations. We start with a discussion based on DFT calculations about surface segregation effects and their relation to the stability of the catalyst surface atoms against dissolution, focusing on core–shell structures with a top platinum monolayer. Then, we refer to the degradation of the catalyst under acid medium as a function of the extent of surface oxidation, on the basis of DFT, ab initio, and classical MD simulations. We finalize by introducing a DFT model for describing reactivity for adsorbates confined within metal pores emulating the structure of the catalyst after dealloying.

2 Surface Segregation and Stability of Core–Shell Alloy Catalysts

It was mentioned in the Introduction that DFT analyses has yielded useful indicators of catalytic activity. In a similar way, we may expect specific properties of the core–shell system to be useful in anticipating stability behavior against dissolution. For example, the atomic size of a given core element, as well as its surface energy and cohesive energy are known to be correlated with its surface

segregation energy [42]. More importantly, under ORR conditions, several oxygenated intermediates will be deposited on the surface, and even migrate to the subsurface of the catalytic particle [56–58]. The presence of these species are driving forces that facilitate surface segregation and induce the first significant changes on the catalytic surface [59]. Therefore the oxophilicity of the core element is crucial. For example, in Pt/Co alloys the stabilization energy when one Pt atom is substituted by one Co atom in vacuum is −0.68 eV and becomes −2.34 eV under 0.25 mL of O adsorbed on the surface [60].

With respect to the stability of Pt surface atoms of the skin-surface systems relative to pure Pt (111), our DFT analysis has shown [60] that core–shell structures with pure substrates of Ir, Au, Rh, Pd, and Ag make the Pt surface atoms more stable on the skin-surface systems than pure Pt (111) surfaces, in vacuum and under 0.25 mL of O adsorbed on the surface, whereas Co, Ni and Cu make the Pt surface less stable against dissolution. In addition, these elements have a large tendency to dissolve in acid medium; their standard reduction potentials with respect to the hydrogen electrode are more negative than that for Pt (1.18 V): −0.28 V for Co, −0.257 V for Ni, and 0.342 V for Cu [61], as shown by previous experimental and DFT studies [48].

Thus, based on the calculated indicators of electrocatalyst stability, none of the 3d-metals (Co, Ni and Cu) would be good substrates or cores since they tend to segregate to the surface and modify its structure, and the Pt skins on these substrates tend to dissolve more than pure Pt [60]. In contrast, the 4 and 5d substrates could stabilize the Pt skin surface against dissolution in vacuum and under O adsorbed. However, only Ir and Pd substrates do not segregate to the surface in vacuum and under 0.25 mL O adsorbed on the surface. Therefore, based on this preliminary analysis, Ir and Pd substrates would be potentially good candidates as core for the Pt skin-surface systems. It is noted that further studies may be needed to investigate the effect of larger oxygen concentrations on the surface, since as shown in the next sections these conditions may be determinant for the posterior evolution of the catalyst.

From the analysis of activity and stability properties, it may be inferred that combining certain 3-d elements with a relatively stable core such as Pd or Ir may provide a successful alloy combination [60]. Stability indicators of Pt/Pd_3X systems, with X = Co, Fe, Cr, V, Ti, Ir, Re are shown in Fig. 1a, b for the surfaces under vacuum and under 0.25 mL of O, respectively. The calculated segregation energies of the substrate atoms to the surface are graphed as a function of the electronic charge of the atom X in the subsurface. The total electronic charge of an atom was calculated using Bader charge analysis [62, 63]. This analysis defines an atom based on the electronic charge density using zero flux surfaces to divide atoms; the total electronic charge of an atom is approximately the charge enclosed within the Bader volume defined by zero flux

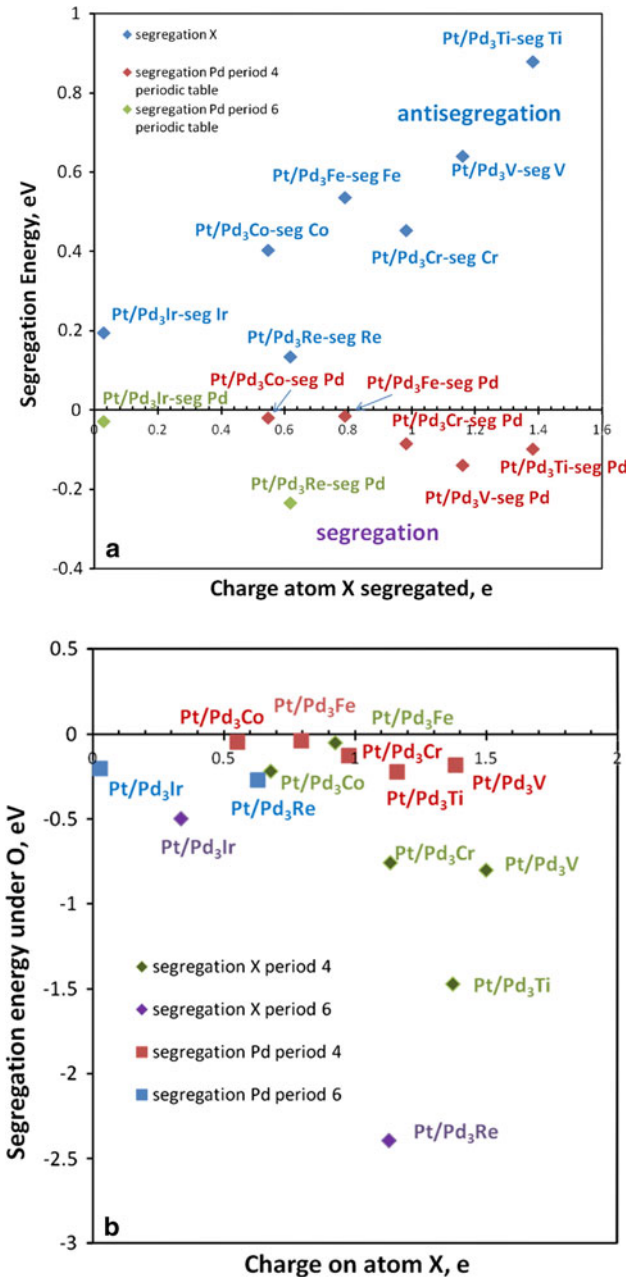

Fig. 1 **a** Segregation energy of X (*blue diamonds*), and segregation energy of Pd (*red diamonds* for X belonging to period 4 and *green diamonds* for X belonging to period 6 of the periodic table) from the core to the surface of *clean* core–shell Pt/Pd_3X alloys, in vacuum. **b** Segregation energy of X (*green diamonds* for X belonging to period 4 and *purple diamonds* for X belonging to period 6 of the periodic table), and segregation energy of Pd (*red squares* for X belonging to period 4 and *blue squares* for X belonging to period 6 of the periodic table) from the core to the surface of core–shell Pt/Pd3X alloys *covered by 0.25 mL of O*. Adapted from [60]; reproduced with permission of the PCCP owner societies

surfaces. Note that *positive* segregation energies indicate destabilization of the system when a given atom migrates to the surface, this is called *antisegregation*. In contrast, *negative* segregation energies signal a more stable system after *segregation* of that species to the surface. Under vacuum, the anti-segregation of X toward the surface increases with the degree of atom X oxidation in the subsurface (positive energies in Fig. 1). Instead, Pd has a slight tendency to segregate to the surface (negative energies in Fig. 1) that also increases with the degree of oxidation of X in the subsurface.

The results in Fig. 1 are organized with respect to X location in the periodic table: period 6 for Ir and Re, and period 4 for the other elements. In both cases the less positively charged Pd atoms tend to segregate to the surface and X atoms tend to remain in the substrate. The positive X atoms establish an attractive electronic interaction with Pt surface atoms which have slightly negative charges; this polarization between the monolayer surface and the substrate layer has been discussed by other researchers based on theoretical and experimental evidence [64, 65]. Under 0.25 mL O adsorbed on the surface (Fig. 1b), Pd segregation trend is similar than in vacuum, however there is a strong segregation of Ir, Cr, V, Ti, and Re, and weaker for Co and Fe. Although Iridium's cohesive properties induce stability of pure Ir substrates such properties may be modified after alloying if Ir atoms may be located in a different atomic environment where their strong antisegregation properties are lost.

A consequence of these substrate segregation results is that the O and OH binding energies are different because of the presence of the segregated atoms on the surface. For example, O binding energies calculated on PtPtPd and PtPtX fcc hollow sites are stronger when Pd atoms are in the surface, but still relatively weak compared to those on pure Pt (111). On the other hand, O binding energies strongly increase under segregation of X, especially in the presence of elements with strong affinity for oxygen, following the order Co < Fe < Ir < Cr < Ti < V < Re. As it will be shown later, the oxygen affinity of substrate elements is not only important to predict the substrate stability but also to design new conceptual structures for better electrocatalysts.

The calculated electrochemical potential shift for the dissolution of Pt surface atoms is presented in Fig. 2. The trends shown reveal a clear correlation between the stability of the Pt atoms against dissolution and the degree of oxidation of the atom X in the subsurface, which support early conclusions about the strong attractive electronic interaction established between the Pt monolayer and the subsurface alloy layer. The calculated binding energies per Pt atom of the monolayer to the substrate increase according to: Ir (−1.29 eV) < Co (−1.33 eV) < Fe (−1.36 eV) < Re

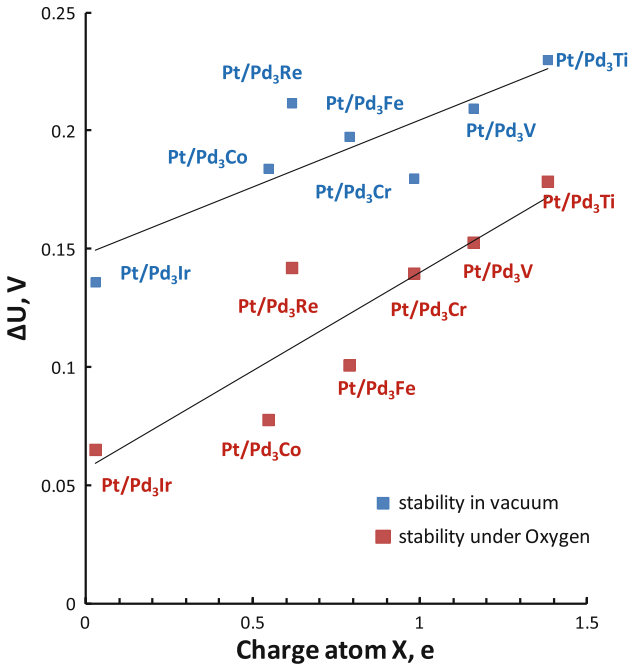

Fig. 2 Electrochemical potential shift for the dissolution of Pt atoms from the surface of the alloys, on clean surfaces (*blue symbols*) and on surfaces covered with 0.25 mL of O (*red symbols*), versus the charge of the atom X in the subsurface of the alloy. Adapted from [60]; reproduced with permission of the PCCP Owner Societies

(−1.53 eV) < V (−1.54 eV) < Ti (−1.56 eV) < Cr (−1.91 eV). With the exception of Cr the order correlates with the stability values of Pt atoms against dissolution in vacuum and under O presented in Fig. 2 [60]. In summary, the presence of a relatively small concentration of X elements in the Pd_3X substrate enhances the stability *of Pt surface atoms* on the skin-surface systems against dissolution, in agreement with previous XPS binding energy shifts [65] and theoretical analysis [64]. We emphasize that the stability described by Fig. 2 refers to the hypothetical case where the core is stable. However, as suggested by Fig. 1b the trend of these elements is to segregate to the surface under 0.25 mL of O. Moreover, any X element that segregates from the core to the surface will dissolve in acid medium following the trend given by their experimental redox potentials [61]. Thus, *all elements* in our study would dissolve at more negative potentials than pure Pt (1.18 V).

The reason of this substrate instability is its strong oxygen affinity that favors surface segregation. A possible solution is to introduce a new structural concept, where the substrate atoms are already oxidized, therefore removing the reason of their segregation to the surface. As an example, we recently discussed a new class of core–shell materials composed of a platinum monolayer over a composite core where an extra element has been added to the core in order to avoid surface segregation of the core

transition metals [66]. More specifically, the system consists of a shell/anchor layer/core structure. The anchor layer in the catalyst is a region that aims to prevent surface segregation of the core metal alloy atoms and their consequent metal dissolution in acid medium. The enhanced substrate stability arises from the use of carbon in the interstitial sites of a thin film (only 2 layers) located in the subsurface that anchors the substrate layers in their positions, impeding their segregation to the surface in vacuum and under O adsorbed while keeping their beneficial properties that favor ORR activity on the top platinum monolayer. The studied systems were: Pt/Fe–C/Ir, Pt/Ni–C/Ir, Pt/Co–C/Ir and Pd/Fe–C/Ir [67]. The main advantages of the proposed materials include O adsorption energies weaker than those on pure Pt surfaces that in general, increase with the number of interstitial carbon atoms in the system. Such increase of the O adsorption energies is due to the expansion of the subsurface lattice in presence of C which affects the Pt–Pt surface distances. However, even in the case of complete filling of the interstitial sites, the O adsorption energies are still weaker than those on pure Pt. In summary, the presence of interstitial C atoms in the anchor region of the composite material results in intermediate adsorption energies thus favoring ORR activity [7, 13]. In addition, segregation of the substrate atoms to the surface under 0.25 mL of O was found to decrease as the number of interstitial C atoms in the anchor region increases. The highest antisegregation energy values were found for the 2:1 metal to carbon ratio. Such behavior can be explained by the oxidant effect of interstitial C on the substrate atoms that significantly reduces their driving force for segregation toward the surface. DFT calculations on these Pt-skin surfaces yielded high stability against dissolution of the Pt surface atoms. We note that the concept has not yet been tested experimentally. Even though the presence of the carbide thin film in the proposed structures may be a challenge for state-of-the-art fabrication techniques, advances in atomic and thin film deposition may make this type of materials feasible in the near future.

3 Catalyst Evolution During Reaction

From the above discussion it may be concluded that the key obstacle for active Pt-based alloy ORR electrocatalysts having reasonably long lifetimes in acid medium is related to the constant evolution of the catalytic surface caused by metal dissolution which is poorly understood in spite of the numerous world-wide research efforts. From the theoretical/computational viewpoint, a multi-scale approach should definitely need to be introduced to achieve an improved understanding. Here we summarize our recent efforts and point out our views on the remaining outstanding challenges.

The dissolution of Pt and other transition metal ions has been observed under highly acidic and oxidizing cathodic environment during PEMFC operation [1, 4, 68]. The dissolved metal cation may be reduced and agglomerate with other metal particles increasing the catalyst particle size or it may migrate through the electrolyte phase to other fuel cell regions [69]. Thus, the study of the catalyst degradation is of primary importance since it impacts the performance of the entire system. The causes and mechanisms of catalyst degradation in the electrodes and metal migration to other fuel cell regions are not fully understood. In the case of pure Pt, experimental results have revealed the existence of a correlation between the degree of surface oxidation and the amount of Pt dissolution [59]. Moreover, the "place exchange" mechanism [70, 71] is often used to explain surface changes associated with the development of a surface oxidation film. During such place exchange it is assumed that adsorbed O atoms may migrate into the subsurface, exchanging locations with Pt atoms, giving place to an irreversible surface roughening called buckling. In this work, buckling is defined as the difference in the z coordinate of a surface atom and that corresponding to the plane of the surface. Buckling of Pt atoms has been revealed by DFT calculations at increasing O coverage [56–58, 72, 73] and by experimental results [72, 74].

Figure 3 shows that buckling is directly related to the Pt–O coordination number. When a Pt atom is coordinated to more than two O atoms (such as Pt atoms, labeled #59 and #63 in Fig. 3) significant buckling is detected, as shown in Table 1.

On the other hand, in a relatively crowded surface as shown in Fig. 4, where there are two oxygenated species O and OH each one with a coverage of 0.33 mL, the maximum buckling found was of 0.29 Å and the maximum charge on a Pt atom was 0.5 e. Note from Fig. 4 that in this case the adsorbate distribution is very symmetric and there is no Pt atom coordinated to more than two oxygenated species.

Buckling is enhanced by oxygen absorption into the subsurface but also by the presence of other species on the surface, for example hydronium ions, or cations and anions from the acid medium [74, 75]. Results from ab initio MD simulations[73] indicate that chloride ions play an important role as additional oxidant agents inducing further increases in buckling effects and oxidation of Pt atoms located in its proximity with respect to other surface atoms. A sequence of events visualized in Fig. 5 illustrates buckling of a Pt atom induced by adsorption of chloride and OH species which are stabilized by the water molecules on the top layer. Hydronium ions decompose into OH

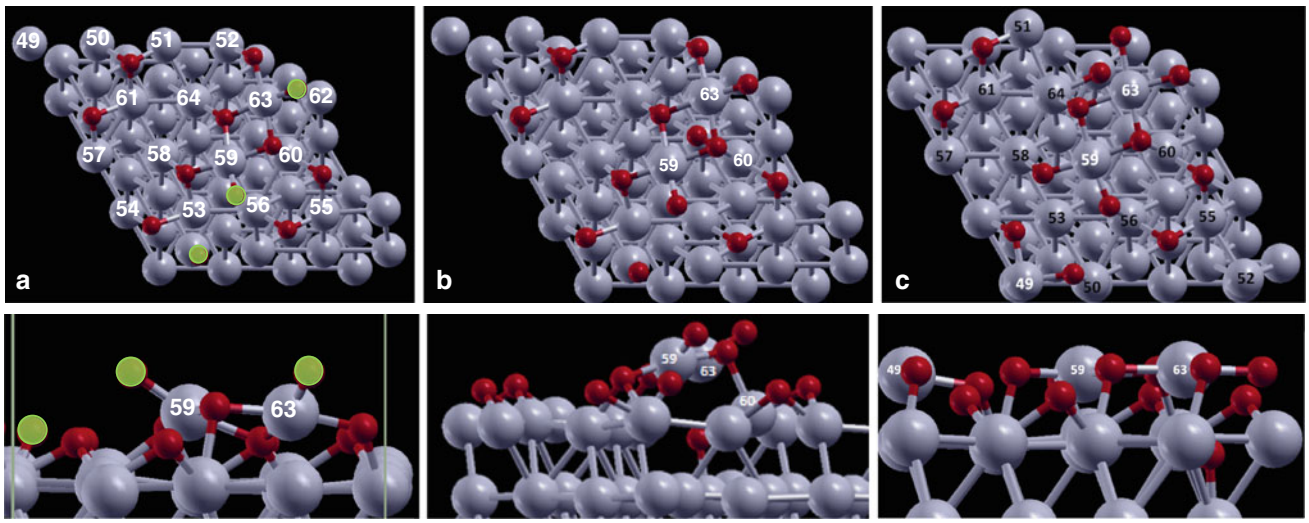

Fig. 3 DFT calculated structures of oxygen adsorption on Pt (111) surfaces at several O coverages. **a** 0.75 mL of O adsorbed on the surface; the three atoms highlighted in green are the ones added to increase the coverage from 0.5625 to 0.75 mL. (**b**, **c**) Two different configurations with total coverage of 0.8125 mL of O (0.75 mL on surface and 0.0625 mL in subsurface). The subsurface O is located in a tetra I site. Buckling and surface reconstruction is visualized in top (*top* images) and side views (*bottom* images)

Table 1 Buckling (in Å) and charge (in e) of topmost atoms of Pt (111) obtained from DFT calculations

Atom ID	0.5625 mL oxygen (not shown)		0.75 mL oxygen (Fig. 4a)		0.8125 mL oxygen (Fig. 4b)		0.8125 mL oxygen (Fig. 4c)	
	Charge (e)	Buckling (Å)	Charge (e)	Buckling (Å)	Charge (e)	Buckling (Å)	Charge (e)	Buckling (Å)
49	0.45	0.02	0.65	0.29	0.66	0.36	**1.08**	**1.73**
50	0.21	−0.08	0.44	−0.06	0.43	−0.05	0.46	−0.03
51	0.46	0.11	0.47	0.12	0.48	0.13	0.50	0.07
52	0.22	−0.09	0.21	−0.10	0.21	−0.08	0.47	0.10
53	0.44	0.02	0.58	0.24	0.56	0.27	0.32	−0.11
54	0.20	−0.10	0.25	−0.17	0.24	−0.17	0.23	−0.08
55	0.49	0.09	0.48	0.02	0.47	0.03	0.47	−0.01
56	0.18	0.02	0.22	−0.07	0.23	−0.05	0.43	−0.03
57	0.49	0.09	0.49	0.02	0.47	0.03	0.51	0.13
58	0.22	−0.09	0.24	−0.09	0.23	−0.08	0.23	−0.08
59	**0.76**	**1.35**	**1.13**	**1.92**	**1.16**	**2.11**	**1.11**	**1.76**
60	0.39	−0.12	0.40	0.01	0.70	0.38	0.43	0.00
61	0.45	0.11	0.47	0.13	0.47	0.12	0.46	−0.02
62	0.18	0.02	0.22	−0.08	0.23	−0.05	0.40	0.01
63	**0.76**	**1.35**	**1.13**	**1.92**	**1.16**	**2.11**	**1.04**	**1.88**
64	0.26	0.02	0.23	−0.13	0.29	−0.07	0.48	0.10

The atom ID corresponds to Fig. 3 and the maximum values of buckling and charge are indicated in bold

and H species, and reforming of HCl molecules is observed (Fig. 5a). In Fig. 5b, a chloride ion is displaced by an OH species. The effect of the hydroxyl formed after proton transfer is similar to that with chloride ion, but the magnitudes of induced buckling and charge transfer are much smaller. These observations are in agreement with experimental results of the enhancement of Pt dissolution when a small amount of HCl is added to an acid medium [76]. The simulations suggested that additional acidic water would be needed to remove the oxidized Pt complexed with other species from the surface.

To further investigate the onset of surface oxidation and its effects on surface structure and composition in much longer time scales than those allowed by ab initio MD simulations, we employed classical MD simulations on pure Pt and Pt alloys, on extended surfaces [77, 78] and on supported nanoparticles [79]. The approach is based on DFT results that suggest that the top three layers of the

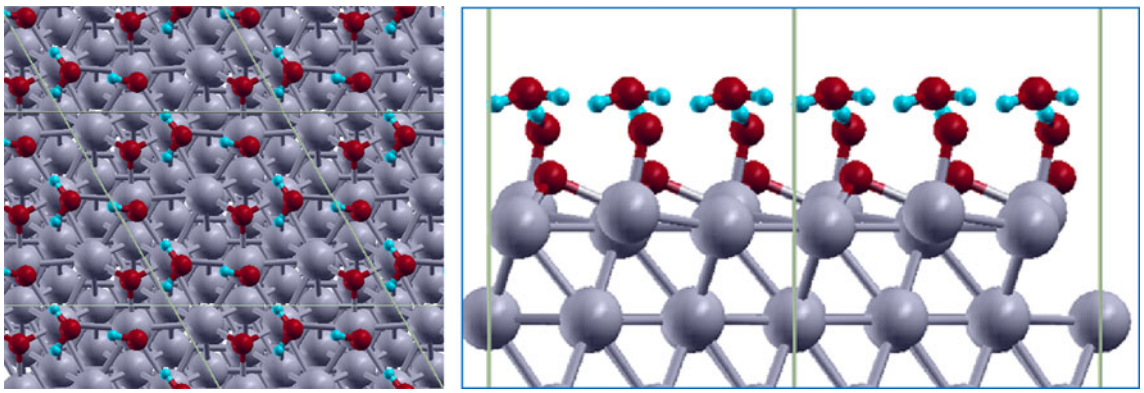

Fig. 4 DFT calculated buckling effects on a surface covered by 0.33 mL of O, 0.33 mL of OH, and 0.3 mL of H_2O. *Red spheres* are O atoms, *blue* ones are H atoms, and grey spheres are Pt atoms

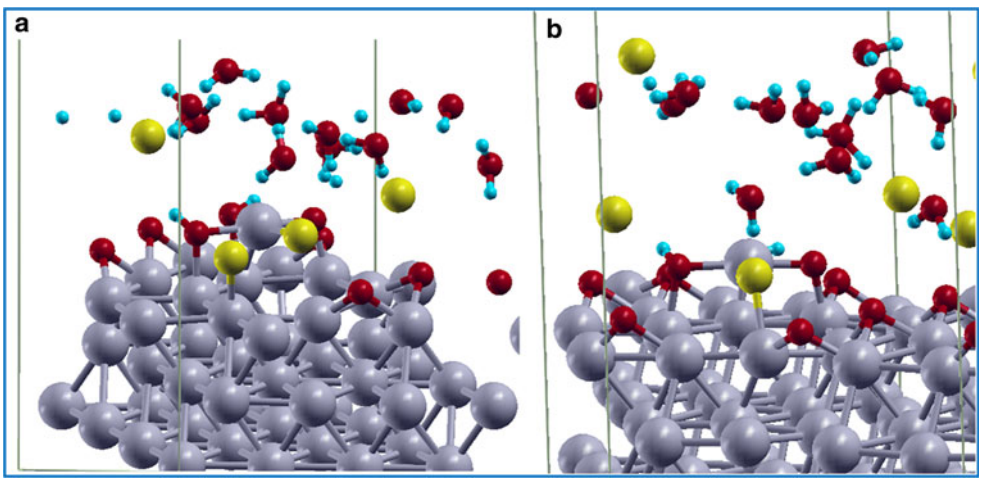

Fig. 5 Ab initio MD results of 0.5625 mL of O adsorbed on Pt (111) in presence of three hydronium and three chloride ions and eight water molecules at 350 K. **a**, **b** are snapshots taken at 0.8 and 1 ps respectively. Adapted from Ref [73] with permission

surface are those that experience the largest structural and electronic changes during oxidation. Thus, the DFT calculated (positive) electrostatic charges on the atoms of the top surface and first subsurface layer are incorporated into the force field that employs a combination of Lennard-Jones and Coulombic terms. Average values of the surface and subsurface charges obtained from DFT were used in the MD simulations. Oxygen molecules were assumed to be already dissociated and the resultant oxygen atoms carry a negative electrostatic charge; the magnitude of the charges on the adsorbate and on the metal correlate with the surface oxidation state, with the total system being electrically neutral. Such oxygen anions interact readily with the charged top surface layers, thus showing adsorption and absorption of O atoms. Solvent effects were incorporated using the modified central force (CF-1) water model [80–82] that allows water dissociation. The model represents water as a molten salt of H^+ and O^- species which combine to form water while allowing the formation of H_3O and OH species. These species are present on the catalyst surface as a result of cathodic and anodic electrochemical reactions that may include water dissociation; however in the simulation they are produced mostly through water dissociation on the surface which becomes more favorable under oxidation conditions. However, hydronium ions from water dissociation are also able to interact with the adsorbed O anions forming OH species capturing at least in part the chemistry of the system. HCl-like molecules were added to the system to represent an acidic environment (pH = 3). The net result is the enhancement of water dissociation under these acidic conditions [77]. The overall aim of these simulations was to detect structural changes on the catalytic surface and dynamics and redistribution of adsorbates (including O, OH, H_2O, H_3O) under a highly oxidizing environment. The simulated systems were Pt (111) and Pt/PtCo/Pt_3Co (111) both in slab geometries and as nanoparticles of an approximate diameter of 4 nm, supported on a graphite substrate. The particular atomic distribution of the alloy used in the initial configuration (Pt/PtCo/Pt_3Co) was adopted on the basis of DFT calculations indicating that this is the most stable configuration of clean Pt_3Co alloys; [83] the result was also reproduced with the chosen force field [78].

Figure 6 illustrates significant changes in the surface morphology due to adsorption of increasing amounts of atomic oxygen. At the lowest O coverage (0.5 mL), O atoms are mostly occupying their preferred hollow sites. However, as the O concentration increases, visible surface buckling and reconstruction takes place due to migration of O atoms into subsurface interstitial sites. In the case of the studied alloys, such reconstruction is mainly caused by

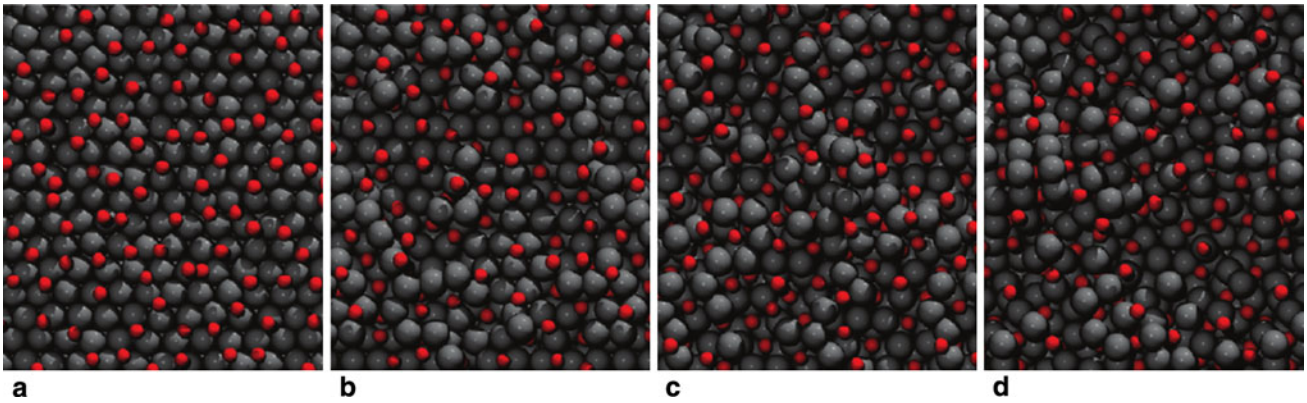

Fig. 6 Results from classical MD simulations for O adsorption on Pt (111) slabs at increasing levels of surface oxidation: **a** 0.5 mL of O; **b** 0.6 mL of O; **c** 0.75 mL of O; **d** 0.85 mL of O and water. Solvent molecules are not shown for clarity. Reprinted with permission from [78]. Copyright 2011, American Chemical Society

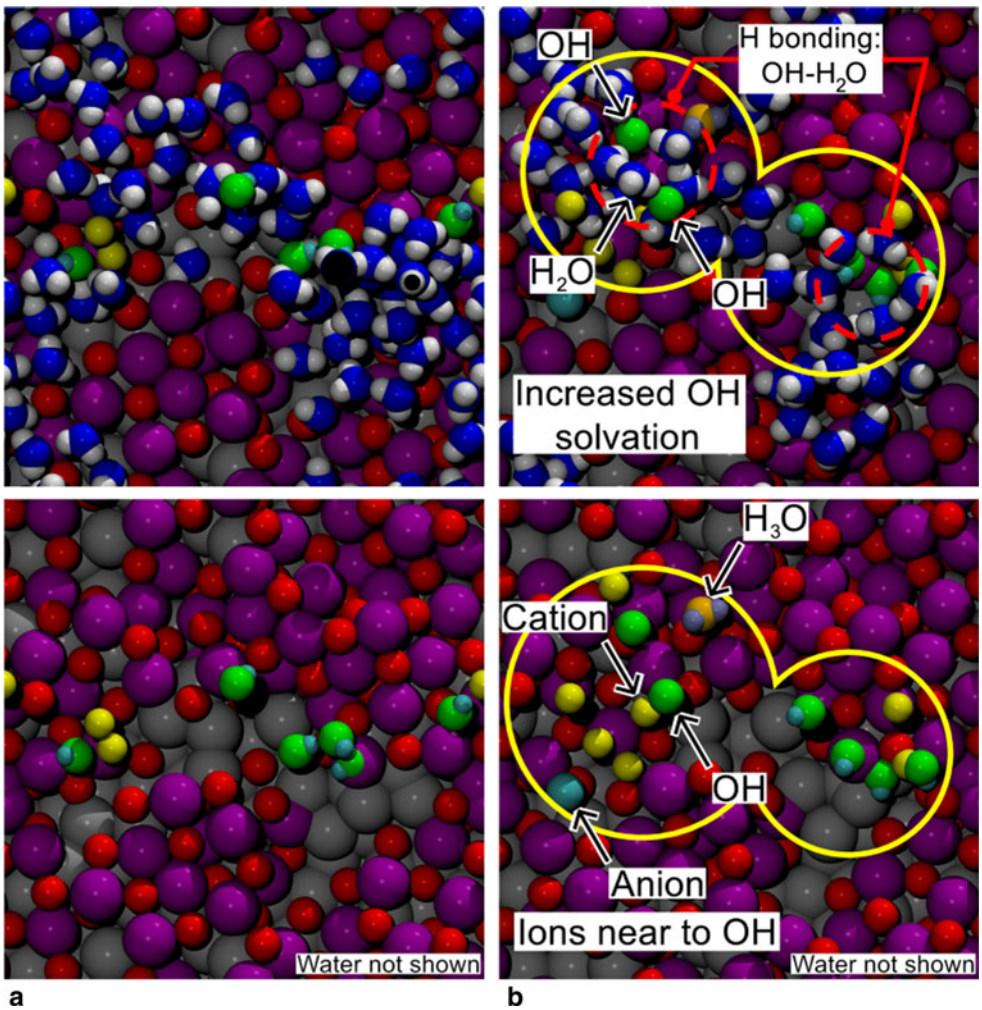

Fig. 7 Snapshots of Pt/PtCo/Pt_3Co (111) surface simulated as a slab under 0.85 mL oxygen and water without acid molecules (**a**) and at pH = 3 (**b**) after 500 ps. The water molecules are not shown in the second row of images. Color key: platinum—*grey*, cobalt—*purple*, oxygen—*red*, cation—*yellow*, OH—*green*, H_2O—*blue* and *white*, H_3O—*orange* and *purple*, anion—*cyan*. Reproduced from [77]; with permission of the PCCP Owner Societies

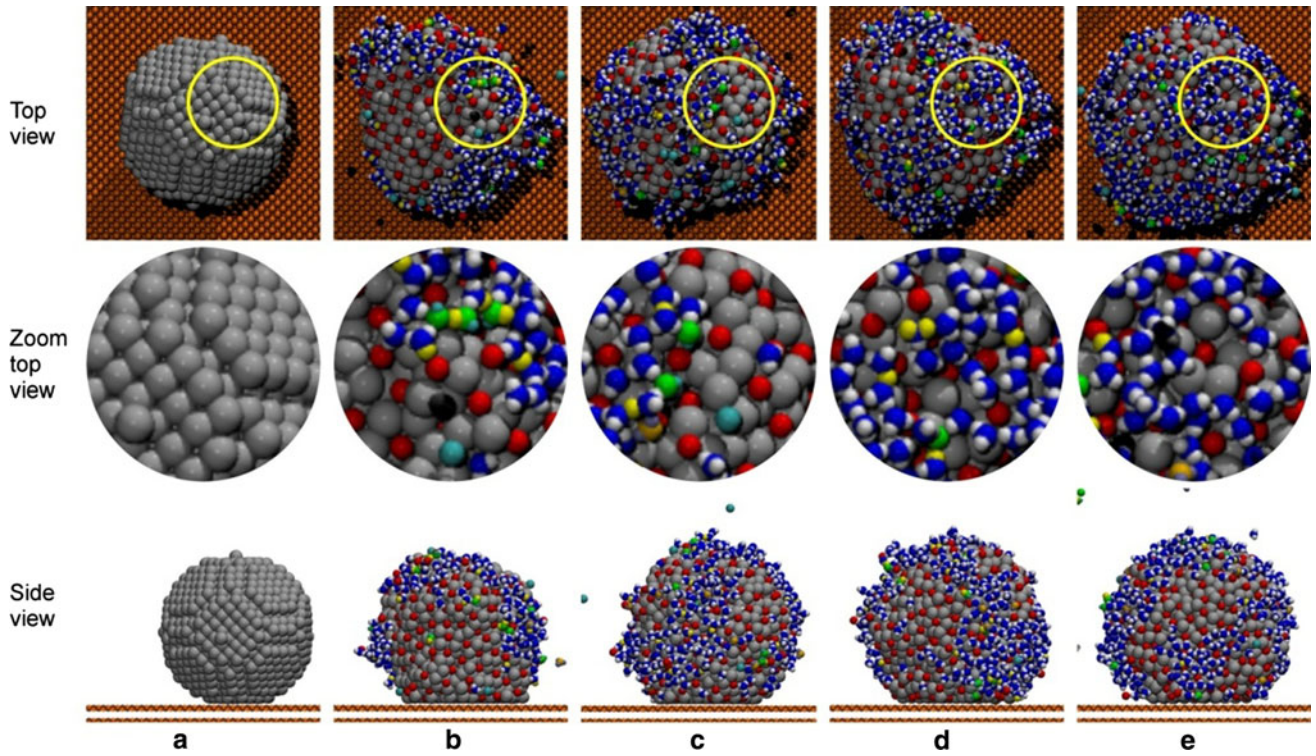

Fig. 8 Snapshots of the C-supported Pt nanoparticle: **a** under vacuum, **b**–**e**: at 0.5, 0.6, 0.75, and 0.85 mL of oxygen and water, taken at the end of the simulation using the CF1 model and under pH = 3. Color key: platinum—*grey*, oxygen—*red*, cation—*yellow*, OH—*green*, H_2O—*blue* and *white*, H_3O—*orange* and *purple*, anion—*cyan*, carbon—*orange*. Reprinted with permission from [79]. Copyright 2011, American Chemical Society

segregation of the non-noble Co atoms towards the surface, leaving vacancies in the subsurface that are readily occupied by Pt atoms; thus surface composition changes to a Co-enriched surface distribution. Some of the most important effects are shown in Fig. 7. The oxygenated species (O and OH) show a strong preference for surface Co and in lesser degree for Pt. Water molecules are observed to agglomerate near OH species forming H-bonding. The phenomena resembles that found experimentally and theoretically on Pd surface oxides [84, 85] where water tends to bond to low-coordinated metal atoms.

The presence of acid molecules causes further water dissociation and therefore more OH and water agglomerations on the surface. Additional simulations were performed using similar approach on a nanoparticle of approximate diameter of 4 nm supported on a model graphite substrate. Figures 8, 9, 10 display snapshots illustrating aspects of the particle degradation due to the oxidation effect. The initial configuration of a pure Pt nanoparticle (2,123 atoms) in Fig. 8a shows typical (111) and (100) facets of a cubo-octahedral cluster. As O and OH are adsorbed on the surface (Fig. 8b–e), the nanoparticle shape becomes more rounded and the facets are gradually lost. The particle changes shape and an enhanced wetting of the substrate is detected as the degree of oxidation increases. The solvation effect causes the formation of small islands of water on the surface, as discussed in relation to the slab surface in Fig. 7.

Similar observations can be done with respect to the evolution of the alloy nanoparticle as shown in Fig. 9. Note that in the initial configuration the nanoparticle exhibits a Pt-skin surface (Fig. 9a), which is gradually changed by migration of Co atoms from the subsurface. Migration of O atoms into subsurface sites is clearly observed in Fig. 9d.

The MD simulations were also used to emulate the effect of cycling: reduction followed by oxidation stages as in a cyclic voltammogram. The reduction effect was obtained by gradually reducing the charges on the surface atoms and on the adsorbates, emulating the effect of the electrochemical potential on the surface and adsorbates. At the end of ten cycles, there was a clear loss of electrochemical surface area, and detachment of surface atoms was also observed [79]. The degradation of the catalytic surface is in excellent agreement with recent experimental observations [68].

In summary, these MD simulations are able to capture some of the important features of the oxidation-driven catalyst degradation, such as buckling, surface restructuring, atomic redistribution, and atomic detachment. However, as the non-noble metals are dissolved in the

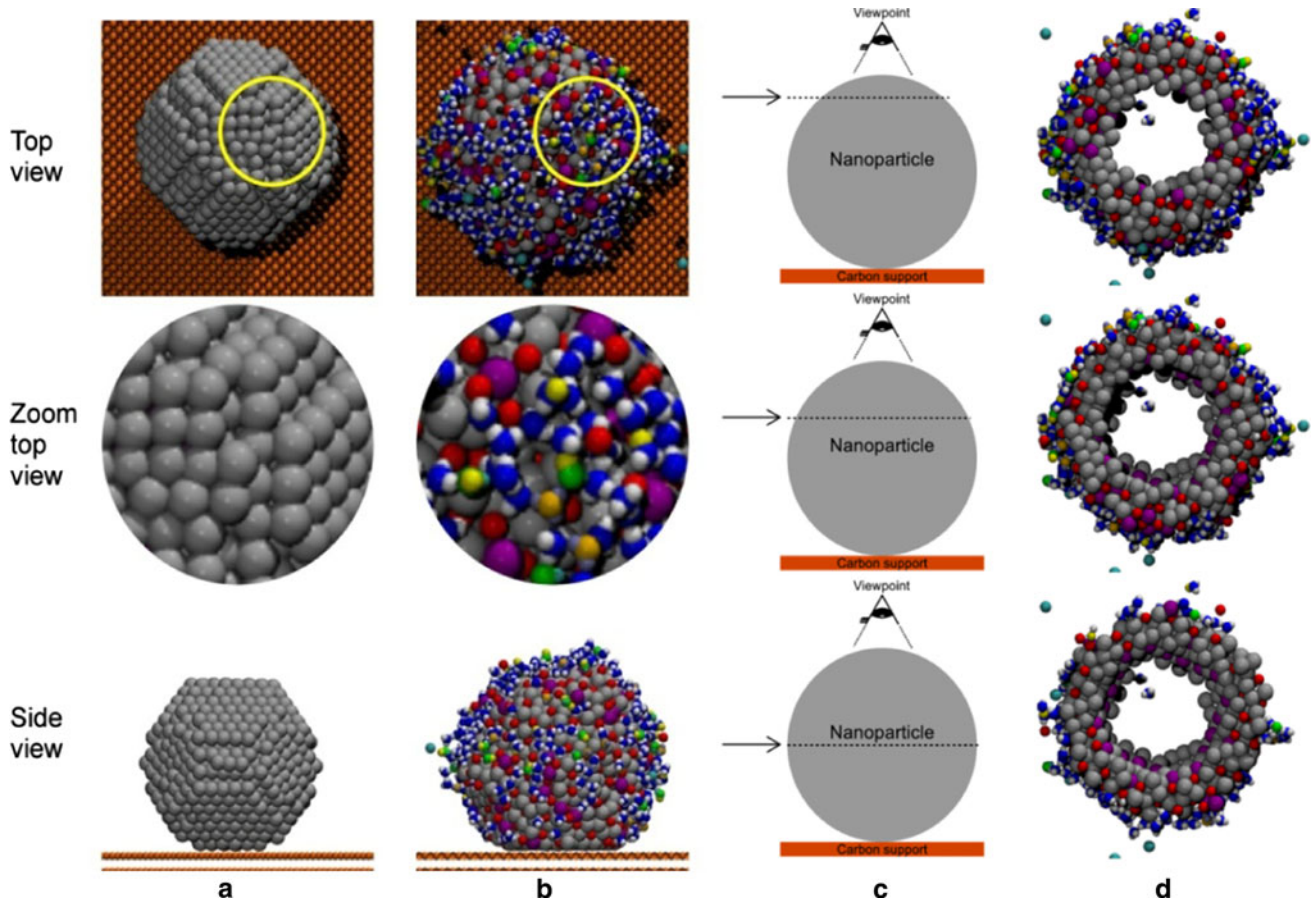

Fig. 9 **a** Snapshots of the C-supported Pt/PtCo/Pt_3Co nanoparticle under vacuum and **b** under 0.6 mL of oxygen and water taken at the end of the simulation using the CF1 model and under pH = 3. **c** Schematic indicating cut of the nanoparticle showing only the shell region. **d** Snapshots of regions within the C-supported Pt/PtCo/Pt_3Co nanoparticle under 0.6 mL of oxygen and water taken at the end of the simulation using the CF1 model and under pH = 3. Only the adsorbates and charged metal atoms are shown. Color key: platinum—*grey*, cobalt—*purple*, oxygen—*red*, cation—*yellow*, OH—*green*, H_2O—*blue* and *white*, H_3O—*orange* and *purple*, anion—*cyan*, carbon—*orange*. Reprinted with permission from [79]. Copyright 2011, American Chemical Society

electrolyte phase, the dealloying process in acid medium have been reported to give rise to hollow structures [48, 86–89] with significantly enhanced activity. Moreover, different nanoporous structures defined as "spongy" [90] or "hollow" [68] have been detected using different dealloying protocols. Simulating the development of such porous structures would require the use of a different method, such as Kinetic Monte Carlo [91]. In addition, DFT may be used to investigate the effect of metal porosity on the catalytic activity. Regarding this point, although not much is known regarding the catalytic structure of a metal porous matrix, it is worth to mention that significant changes in the catalytic effects have been detected when molecules are confined within surfaces separated by nanometer distances [92–94]. This effect is a consequence of the geometric and electronic changes given in the reaction environment. In the next section we briefly summarize our results and discuss them in the context of ORR reactivity.

4 Metallic Porous Structures and the Confinement Effect on Reactivity

The proximity of two transition-metal surfaces separated by a gap of molecular dimensions gives rise to strong interactions that could be potentially useful for enhanced reactivity in catalysis, separations, and sensing processes [95, 96]. Depending on the nature of the interacting surfaces, confined adsorbates may be strongly adsorbed, dissociated, or reacted with other species [97]. Separation of mixed gases or liquids could be obtained by appropriately tuning the composition of the alloy surfaces and the gap geometry [98]. Furthermore, the importance of local atomic disorder on reactivity has been pointed out based on X-Ray absorption spectroscopy experiments [99]. Recently we have studied the activity improvement on the dissociation of molecular oxygen confined between Pt surfaces separated by a short distance. We found that at certain Pt surface–surface separation, the dissociation of molecular

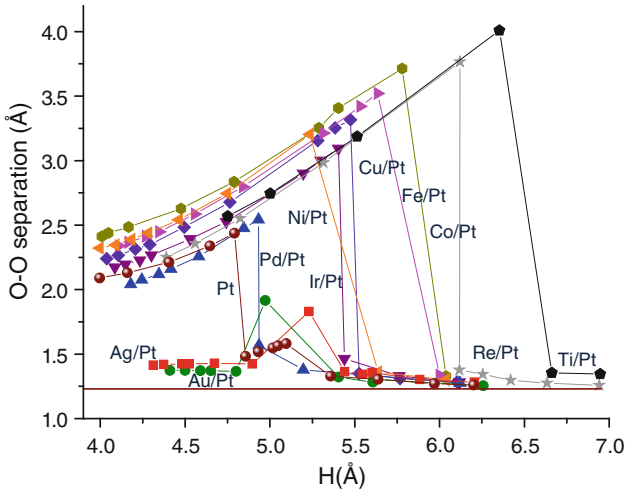

Fig. 10 Spontaneous molecular oxygen dissociation occurs in skin-surfaces (X/Pt, X = Pd, Cu, Ir, Ni, Fe, Co, Re, Ti) as the surface–surface separation H is decreased, as evidenced by the sudden change in OO bond length, except on Au/Pt and Ag/Pt where there is O–O elongation without complete dissociation. Taken from Ref. [101], reproduced with permission of the PCCP Owner Societies

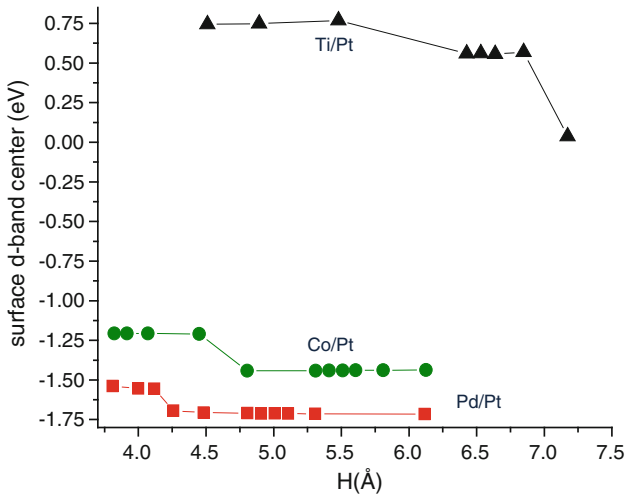

Fig. 11 Electronic structure changes in the surface valence bands illustrated by the variation of the surface d-band center as a function of surface–surface separation. For the case of Co/Pt and Pd/Pt surfaces at short surface–surface separations the d-band center is closer to the Fermi level leading to a higher surface activity. Taken from Ref. [101] reproduced with permission of the PCCP Owner Societies

oxygen is spontaneous [100]. We also studied interactions of X/Pt skin surfaces where X is a monolayer of a 3, 4, or 5d metal. In this case, the effect of the separation distance between X/Pt surfaces was analyzed in relation to the dissociation of molecular oxygen and water (Fig. 10). It was found that the electronic structure of skin surfaces under confinement changes with respect to that of a single surface, becoming more active for catalysis [101]. Changes in the electronic structure of the confined skin surfaces can

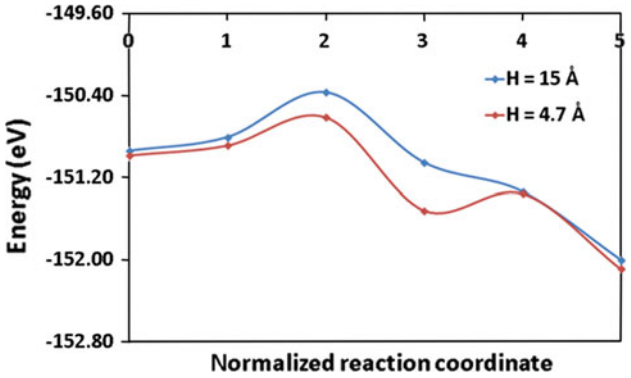

Fig. 12 Energy pathway for the dissociation of the chemisorbed O_2 molecule on the Pt (111) surface, for surface = surface separations $H = 4.7$ and 15 Å. Reprinted with permission from [104]. Copyright 2011, American Chemical Society

be detected on other physical properties such as magnetic moments [102]. The influence of the overlayer metal nature on these phenomena offers the possibility to design specific materials for targeted catalytic applications by manipulation of control variables, such as the surface–surface separation between the skin surfaces but also the composition of the composite system [101]. For example, the interaction between Ti/Pt surfaces separated by a small gap in the order of 0.4–0.8 nm facilitates the creation of a gas of electrons in the gap between surfaces inducing the formation of an ethylene radical that readily reacts with another ethylene radical and starts polymerization without the need of an initiator [103].

Evidently, significant electronic changes take place on the composite systems, as indicated by the changes in the d-band center of the surface atoms as a function of the surface–surface separation shown in Fig. 11.

The results shown in Fig. 10 correspond to the spontaneous dissociation of the O_2 molecule initially located with its OO bond perpendicular with respect to the surface planes [101]. In that case, each of the O atoms receives electrons from each of the interacting surfaces, with the electrons in the gap further contributing to a barrierless dissociation. On the other hand, if the initial position of the O_2 molecule is closer to one of the surfaces, adsorption is most favorable on bridge position, and the dissociation takes place on one of the surfaces. However, as the two surfaces become closer to each other, the barrier for dissociation reduces significantly, as shown in Fig. 12, where the calculated barriers are 0.37 and 0.57 eV for surface–surface separations of 4.7 and 15 Å respectively [104]. The reduced activation barrier for the 4.7 Å surface–surface separation is induced by the electronic and geometric confinement effect on the reaction pathway. The geometries of the adsorbates along the initial, intermediates, and final states, are shown in Fig. 13, corresponding to the energies of Fig. 12.

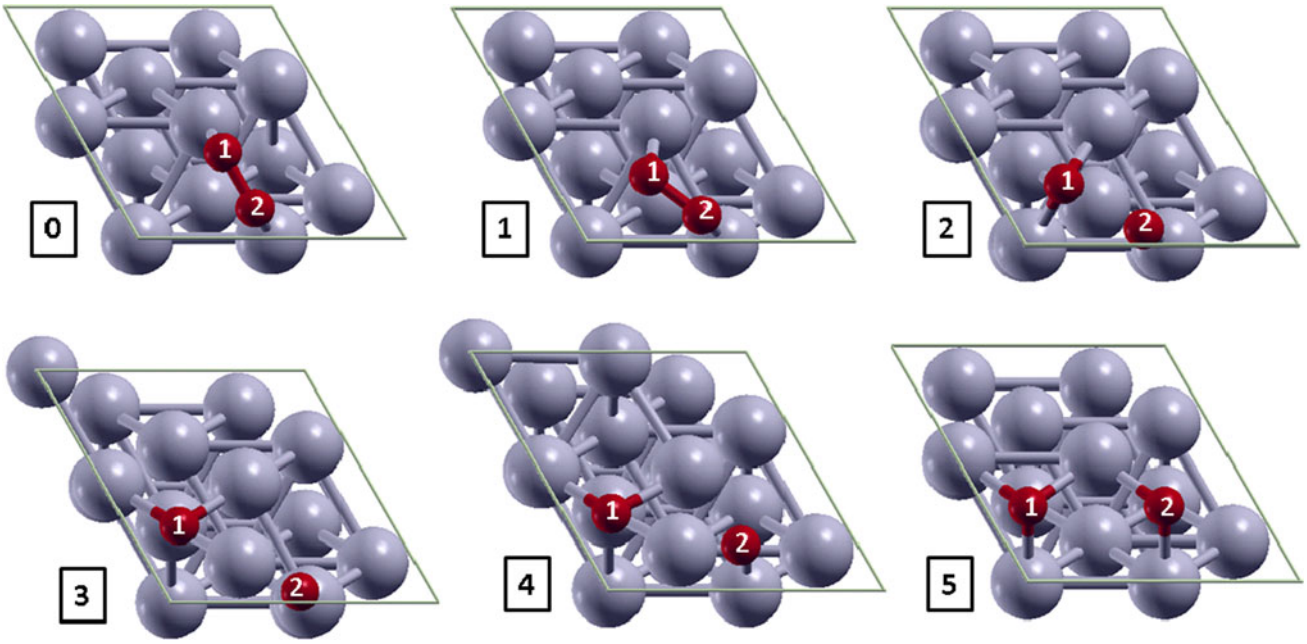

Fig. 13 Geometries of initial state (0), intermediate states (*1–4*), and final state (*5*) for a surface–surface separation $H = 4.7$ Å. The numbers *0–5* correspond to the states displayed in Fig. 12. Reprinted with permission from [104]. Copyright 2011, American Chemical Society

Table 2 Bond lengths between the O atoms, and from the O atoms to the closest surface Pt atoms

Image number	Bond length (Å)					
	$H = 15$ Å			$H = 4.7$ Å		
	O–O	Pt–O1	Pt–O2	O–O	Pt–O1	Pt–O2
0	1.35	2.05	2.05	1.40	2.03	2.03
1	1.37	2.08	2.03	1.40	2.07	2.06
2	1.91	2.03	1.89	1.81	2.06	1.95
3	2.94	2.06	1.84	3.07	2.06	1.91
4	2.72	2.01	1.92	2.92	2.04	1.93
5	2.80	2.03	2.03	2.80	2.04	2.04

Image numbers and atom labels correspond to Fig. 12

The geometrical parameters (bond lengths and bond distances) between adsorbates and from the adsorbates to the surface are listed in Table 2. Note that the longer value of the surface–surface separation distance (15 Å) represents the limit of only one surface interacting with the molecule. Figure 12 illustrates that in the confined state ($H = 4.7$ Å), there is an initial barrier for the formation of a chemisorbed state with elongated OO distance (state 1), with a possible transition state geometry displayed in state 2 (Fig. 13) where the OO distance is already longer than those of the dissociation precursors (Table 2). The next step is a minimum in energy (state 3); the molecule is totally dissociated but the atoms are not yet in their optimal positions. Thus, the geometry evolves to a new transition state (state 4) and finally to a state of minimal energy (state 5) where the two O atoms occupy hollow sites.

This simple example illustrates the potential effect of confinement on the ORR. Many other intermediate steps such as coupled proton and electron transfers to the oxygenated species could be equally affected by such geometric and electronic confinement, as suggested by the recent work of Erlebacher and coworkers [105], where a nanoporous structure obtained after dealloying and filled by an ionic liquid yields a significant activity improvement in the ORR. In our example, the two interacting surfaces represent the geometry of a slit pore, which could be induced by dealloying effects leading into porous structures. In agreement with the findings of Erlebacher et al. we suggest that confinement-induced electronic effects present in such structures should be the source of the enhanced reactivity. Since several other recent reports have also indicated improved ORR activities and stabilities after dealloying [86, 88], it is clear that more work is needed in order to assess the origins of such activity and stability. Coarse grained Kinetic Monte Carlo methods [91] where prefactors and activation barriers of the main events are

obtained with DFT and classical molecular dynamics simulations, may help to identify details about the catalytic structures after the dealloying process. Once such structures are elucidated, DFT models can be used to determine the causes of the enhanced activity and to guide catalytic treatments or suggest new designs.

5 Summary

A combination of enhanced activity and sustained durability is required for the success of Pt-based alloys as efficient ORR electrocatalysts. Such alloys are primarily designed using cheap non-noble metals in the core to reduce the amount of Pt utilized and the overall cost of the catalyst, while keeping and sometimes enhancing the ORR catalytic activity. However, the strong oxygen affinity of the non-noble atoms (Co, Ni, Fe, and others) facilitates their migration to the surface where they become easily dissolved in acid medium. Moreover, the catalyst surface and its overall structure result significantly modified especially at conditions where oxidation starts to take place, due to surface restructuring mainly caused by oxygen migration into the subsurface and non-noble metals migrating towards the surface and detaching in acid medium. These changes are especially important in nanoparticles where nanoporous structures may arise as a consequence of dealloying. It is interesting that such metal nanoporous structures are found to be significantly stable and active. We suggest that the origin of such enhanced activity may be related to the presence of void spaces where molecules could be exposed to electronic changes induced by interacting metal surfaces separated by short distances resulting in a net reactivity benefit.

Acknowledgments This work is supported by the Department of Energy, grant DE-FG02-05ER15729. Computational resources from Texas A&M University Supercomputer center, from the National Energy Research Scientific Computing Center, which is supported by the Office of Science of the U.S. Department of Energy under Contract No. DE-AC03-76SF00098, and from the University of Texas at Austin TACC system are gratefully acknowledged.

References

1. Yu XW, Ye SY (2007) J Power Sources 172:133–144
2. Antolini E (2003) J Mater Sci 38:2995–3005
3. Shao YY, Yin GP, Gao YZ (2007) J Power Sources 171:558–566
4. Gasteiger HA, Kocha SS, Sompalli B, Wagner FT (2005) Appl Cat B 56:9–35
5. Peng ZM, Yang H (2009) Nano Today 4:143–164
6. Greeley J, Mavrikakis M (2004) Nat Mat 3:810–815
7. Greeley J, Stephens IEL, Bondarenko AS, Johansson TP, Hansen HA, Jaramillo TF, Rossmeisl J, Chorkendorff I, Norskov JK (2009) Nat Chem 1:552–556
8. Greeley J, Norskov JK, Mavrikakis M (2002) Ann Rev Phys Chem 53:319–348
9. Norskov JK, Scheffler M, Toulhoat H (2006) MRS Bull 31:669–674
10. Hyman MP, Medlin JW (2007) J Phys Chem C 111: 17052–17060
11. Kitchin JR, Reuter K, Scheffler M (2008) Phys Rev B 77:075437
12. Zhang J, Vukmirovic MB, Xu Y, Mavrikakis M, Adzic RR (2005) Angew Chem Int Ed 44:2132–2135
13. Wang Y, Balbuena PB (2005) J Phys Chem B 109:18902–18906
14. Xu Y, Ruban AV, Mavrikakis M (2004) J Am Chem Soc 126:4717–4725
15. Norskov JK, Rossmeisl J, Logadottir A, Lindqvist L, Kitchin JR, Bligaard T, Jonsson H (2004) J Phys Chem B 108:17886–17892
16. Sidik RA, Anderson AB (2002) J Electroanal Chem 528:69–76
17. Panchenko A, Koper MTM, Shubina TE, Mitchell SJ, Roduner E (2004) J Electrochem Soc 151:A2016–A2027
18. Balbuena PB, Altomare D, Agapito LA, Seminario JM (2003) J Phys Chem B 107:13671–13680
19. Balbuena PB, Altomare D, Vadlamani N, Bingi S, Agapito LA, Seminario JM (2004) J Phys Chem A 108:6378–6384
20. Jacob T, Muller RP, Goddard I WA (2003) J Phys Chem B 107:9465–9476
21. Wang Y, Balbuena PB (2005) J Chem Theory Comp 1:935–943
22. Wang Y, Balbuena PB (2004) J Phys Chem B 108:4376–4384
23. Wang Y, Balbuena PB (2005) J Phys Chem B 109:14896–14907
24. Roques J, Anderson AB (2005) Surf Sci 581:105–117
25. Roques J, Anderson AB, Vivek SM, Mukerjee S (2005) J Electrochem Soc 152:E193–E199
26. Kitchin JR, Norskov JK, Barteau MA, Chen JG (2004) J Chem Phys 120:10240–10246
27. Xu Y, Mavrikakis M (2002) Surf Sci 505:369
28. Xu Y, Mavrikakis M (2002) J Chem Phys 116:10846–10853
29. Nilekar AU, Xu Y, Zhang J, Vukmirovic M, Sasaki K, Adzic RR, Mavrikakis M (2007) Top Catal 46:276–284
30. Nilekar AU, Mavrikakis M (2008) Surf Sci 602:L89–L94
31. Schnur S, Gross A (2011) Catal Today 165:129–137
32. Taylor CD, Wasileski SA, Filhol JS, Neurock M (2006) Phys Rev B 73
33. Rossmeisl J, Norskov JK, Taylor CD, Janik MJ, Neurock M (2006) J Phys Chem B 110:21833–21839
34. Chen S, Sheng WC, Yabuuchi N, Ferreira PJ, Allard LF, Shao-Horn Y (2009) J Phys Chem C 113:1109–1125
35. Ferreira PJ, Ia OGJ, Shao-Horn Y, Morgan D, Makharia R, Kocha S, Gasteiger HA (2005) J Electrochem Soc 152:A2256–A2271
36. Keith JA, Jerkiewicz G, Jacob T (2010) Chem Phys Chem 11:2779–2794
37. Kleis J, Greeley J, Romero NA, Morozov VA, Falsig H, Larsen AH, Lu J, Mortensen JJ, Dulak M, Thygesen KS, Norskov JK, Jacobsen KW (2011) Catal Lett 141:1067–1071
38. Tritsaris GA, Greeley J, Rossmeisl J, Norskov JK (2011) Catal Lett 141:909–913
39. Chen JG, Menning CA, Zellner MB (2008) Surf Sci Rep 63:201–254
40. Menning CA, Chen JG (2008) J Chem Phys 128:164703
41. Menning CA, Hwu HH, Chen JGG (2006) J Phys Chem B 110:15471–15477
42. Ruban AV, Skriver HL, Norskov JK (1999) Phys Rev B 59:15990–16000
43. Stamenkovic V, Schmidt TJ, Ross PN, Markovic NM (2003) J Electroanal Chem 554–555:191–199
44. Ma Y, Balbuena PB (2008) Surf Sci 602:107–113
45. Ma Y, Balbuena PB (2009) Surf Sci 603:349–353
46. Greeley J, Norskov JK (2007) Electrochim Acta 52:5829–5836

47. Ma Y, Balbuena PB (2008) J Phys Chem C 112:14520–14528
48. Strasser P, Koh S, Greeley J (2008) Phys Chem Chem Phys 10:3670–3683
49. Adzic RR, Zhang J, Sasaki K, Vukmirovic MB, Shao M, Wang JX, Nilekar AU, Mavrikakis M, Valerio JA, Uribe F (2007) Top Catal 46:249–262
50. Vukmirovic MB, Zhang J, Sasaki K, Nilekar AU, Uribe F, Mavrikakis M, Adzic RR (2007) Electrochim Acta 52: 2257–2263
51. Shao MH, Sasaki K, Liu P, Adzic RR (2007) Int J Res Phys Chem Chem Phys 221:1175–1190
52. Zhang J, Vukmirovic MB, Sasaki K, Nilekar AU, Mavrikakis M, Adzic RR (2005) J Am Chem Soc 127:12480–12481
53. Stamenkovic VR, Fowler B, Mun BS, Wang G, Ross PN, Lucas CA, Markovic NM (2007) Science (Washington, DC, United States) 315:493–97
54. Stamenkovic VR, Mun BS, Arenz M, Mayrhofer KJJ, Lucas CA, Wang G, Ross PN, Markovic NM (2007) Nat Mater 6:241–247
55. Kitchin JR, Norskov JK, Barteau MA, Chen JG (2004) Phys Rev Lett 93:156801
56. Gu Z, Balbuena PB (2007) J Phys Chem C 111:9877–9883
57. Gu Z, Balbuena PB (2007) J Phys Chem C 111:17388–17396
58. Gu Z, Balbuena PB (2008) J Phys Chem C 112:5057–5065
59. Wang XP, Kumar R, Myers DJ (2006) Electrochem Sol St Lett 9:A225–A227
60. Ramirez-Caballero GE, Ma Y, Callejas-Tovar R, Balbuena PB (2010) Phys Chem Chem Phys 12:2209–2218
61. Lide DR (2009) CRC handbook of chemistry and physics, 89th edn. Taylor and Francis, Boca Raton
62. Henkelman G, Arnaldsson A, Jónsson H (2006) Comput Mater Sci 36:354–360
63. Sanville E, Kenny SD, Smith R, Henkelman G (2007) J Comput Chem 28:899–908
64. Hennig D, Ganduglia-Pirovano MV, Scheffler M (1996) Phys Rev B 53:10344–10347
65. Liu G, St. Clair TP, Goodman DW (1999) J Phys Chem B 103:8578–8582
66. Ramirez-Caballero GE, Balbuena PB (2010) J Phys Chem Lett 1:724–728
67. Ramirez-Caballero GE, Hirunsit P, Balbuena PB (2010) J Chem Phys 133:134705
68. Dubau L, Durst J, Maillard F, Guetaz L, Chatenet M, Andre J, Rossinot E (2011) Electrochim Acta 56:10658–10667
69. Chen C, Levitin G, Hess DW, Fuller TF (2007) J Power Sources 169:288–295
70. Nagy Z, You H (2002) Electrochim Acta 47:3037–3055
71. Conway BE (1995) Prog Surf Sci 49:331–452
72. Hawkins JM, Weaver JF, Asthagiri A (2009) Phys Rev B 79:13
73. Martinez-De La Hoz JM, Leon-Quintero DF, Hirunsit P, Balbuena PB (2010) Chem Phys Lett 498:328–333
74. Bjorling A, Herrero E, Feliu JM (2011) J Phys Chem C 115:15509–15515
75. Bandlow J, Kaghazchi P, Jacob T, Papp C, Trankenschuh B, Streber R, Lorenz MPA, Fuhrmann T, Denecke R, Steinruck HP (2011) Phys Rev B 83
76. Mitsushima S, Koizumi Y, Uzuka S, Ota K-I (2008) Electrochim Acta 54:455–460
77. Callejas-Tovar R, Balbuena PB (2011) Phys Chem Chem Phys 13:20461–20470
78. Callejas-Tovar R, Liao W, Martinez De La Hoz JM, Balbuena PB (2011) J Phys Chem C 115:4104–4113
79. Callejas-Tovar R, Liao W, Mera H, Balbuena PB (2011) J Phys Chem C 115:23768–23777
80. Arthur JW, Haymet ADJ (1998) Fluid Phase Equilib 150:91–96
81. Arthur JW, Haymet ADJ (1999) J Chem Phys 110:5873–5883
82. Duh DM, Perera DN, Haymet ADJ (1995) J Chem Phys 102:3736–3746
83. Hirunsit P, Balbuena PB (2009) Surf Sci 603:911–919
84. Kan HH, Colmyer RJ, Asthagiri A, Weaver JF (2009) J Phys Chem C 113:1495–1506
85. Kan HH, Weaver JF (2009) Surf Sci 603:2671–2682
86. Mani P, Srivastava R, Strasser P (2011) J Power Sources 196:666–673
87. Yang RZ, Leisch J, Strasser P, Toney MF (2010) Chem Mater 22:4712–4720
88. Shao MH, Shoemaker K, Peles A, Kaneko K, Protsailo L (2010) J Am Chem Soc 132:9253–9255
89. Erlebacher J, Aziz MJ, Karma A, Dimitrov N, Sieradzki K (2001) Nature 410:450–453
90. Chen S, Gasteiger HA, Hayakawa K, Tada T, Shao-Horn Y (2010) J Electrochem Soc 157:A82–A97
91. Policastro SA, Carnahan JC, Zangari G, Bart-Smith H, Seker E, Begley MR, Reed ML, Reynolds PF, Kelly RG (2010) J Electrochem Soc 157:C328–C337
92. Ding Y, Kim YJ, Erlebacher J (2004) Adv Mater 16:1897
93. Snyder J, Asanithi P, Dalton AB, Erlebacher J (2008) Adv Mater 20:4883
94. El-Sayed M (2001) Acc Chem Res 34:257–264
95. Aballe L, Barinov A, Stojic N, Binggeli N, Mentes TO, Locatelli A, Kiskinova M (2010) J Phys Condens Mater 22:015001
96. Li QX, Simon SL (2009) Macromolecules 42:3573–3579
97. Borgoo A, Tozer DJ, Geerlings P, De Proft F (2009) Phys Chem Chem Phys 11:2862–2868
98. Aballe L, Barinov A, Locatelli A, Heun S, Kiskinova M (2004) Phys Rev Lett 93:196103
99. Principi E, Witkowska A, Dsoke S, Marassi R, Di Cicco A (2009) Phys Chem Chem Phys 11:9987–9995
100. Ramirez-Caballero GE, Balbuena PB (2009) J Phys Chem C 113:7851–7856
101. Ramirez-Caballero GE, Balbuena PB (2010) Phys Chem Chem Phys 12:12466–12471
102. Ramirez-Caballero GE, Balbuena PB (2010) Chem Phys Lett 507:117–121
103. Ramirez-Caballero GE, Mathkari A, Balbuena PB (2011) J Phys Chem C 115:2134–2139
104. Martinez de la Hoz JM, Balbuena PB (2011) J Phys Chem C 115:21324–21333
105. Snyder J, Fujita T, Chen MW, Erlebacher J (2010) Nat Mater 9:904–907